Nuclear Instruments and Methods in Physics Research A 743 (2014) 30–38

Contents lists available at ScienceDirect

Nuclear Instruments and Methods in Physics Research A

journal homepage: www.elsevier.com/locate/nima

Development of a SiPM-based PET imaging system for small animals

Yanye Lu [a], Kun Yang [b,*], Kedi Zhou [a], Qiushi Zhang [a], Bo Pang [a], Qiushi Ren [a,**]

[a] Department of Biomedicine and Engineering, College of Engineering, Peking University, Beijing 100871, China
[b] Department of Control Technology and Instrumentation, College of Quality and Technical Supervision, Hebei University, Baoding, 071000, China

ARTICLE INFO

Article history:
Received 23 April 2013
Received in revised form
8 January 2014
Accepted 8 January 2014
Available online 18 January 2014

Keywords:
Geiger-mode APD
LYSO
Instrumentation
Animal imaging

ABSTRACT

Advances in small animal positron emission tomography (PET) imaging have been accelerated by many new technologies such as the successful incorporation of silicon photomultiplier (SiPM). In this paper, we have developed a compact, lightweight PET imaging system that is based on SiPM detectors for small animals imaging, which could be integrated into a multi-modality imaging system. This PET imaging system consists of a stationary detector gantry, a motor-controlled animal bed module, electronics modules, and power supply modules. The PET detector, which was designed as a multi-slice circular ring geometry of 27 discrete block detectors, is composed of a cerium doped lutetium–yttrium oxyorthosilicate (LYSO) scintillation crystal and SiPM arrays. The system has a 60 mm transaxial field of view (FOV) and a 26 mm axial FOV. Performance tests (e.g. spatial resolution, energy resolution, and sensitivity) and phantom and animal imaging studies were performed to evaluate the imaging performance of the PET imaging system. The performance tests and animal imaging results demonstrate the feasibility of an animal PET system based on SiPM detectors and indicate that SiPM detectors can be promising photodetectors in animal PET instrumentation development.

1. Introduction

Positron emission tomography (PET) is a nuclear medicine imaging technology that produces a three-dimensional functional image on the body. The PET imaging system detects two back-to-back 511 keV gamma photons produced simultaneously following positron–electron annihilation by a positron-emitting radionuclide (tracer). The tracer is introduced into the body via a radionuclide conjugated to a biologically active molecule. Advances in PET imaging have accelerated recently due to the development of a number of new technologies along with the use of small animal models in the basic and pre-clinical sciences [1–6]. Silicon photomultiplier (SiPM, also called a multicell Geiger-mode avalanche photodiode) is a solid-state semiconductor photo sensor [7]. Each photon gives the same output signal where the strength is determined by the number of triggered APDs [8]. Compared with a photo multiplier tube (PMT), the SiPM detector has superior attributes such as high photon detection efficiency, compact size, insensitivity to magnetic fields, and low operating voltage; in addition, the quantum efficiency (~25%) and gain (~10^6) are similar to traditional PMTs [9–11]. The cerium-doped lutetium yttrium orthosilicate ($Lu_xY_{2-x}SiO_5$:Ce, LYSO) scintillators are typical scintillators of choice for PET SiPM detectors. The LYSO scintillators exhibit several advantages including high light output and density, excellent energy resolution with quick decay time, no hygroscopic characteristics, and good stability. However, because Lu-based scintillators contain natural radioactivity from the decay of ^{176}Lu into ^{176}Hf, the background counts of LYSO scintillators are considerably higher compared with other scintillators [12].

In recent years, SiPMs have been successfully incorporated into some small animal PET scanners [13–18], and several small animal PET imaging prototypes [19–21] based on SiPM detectors have been developed. The results of these PET imaging prototypes have indicated that SiPMs have the necessary capabilities to be used in PET imaging devices. Our research group has been developing a multi-modality imaging system for preclinical studies. This system composes one anatomical imaging modality (i.e., X-ray computed tomography) and three major molecular imaging modalities [i.e., PET, single photon emission computed tomography (SPECT) and fluorescence molecular imaging (FMI)]. As an important part of the multi-modality imaging system, the PET system must be designed modularly and compactly, which means employing SiPMs is the best choice. The PET detector module is designed with a multi-slice circular ring geometry of discrete block detectors that are composed of LYSO and SiPM arrays. The electronic modules, which include the circuitry for pulse shaping, timing measurement, coincidence-detection, and communication dedicated to the PET imaging system were designed and fabricated. In addition, performance tests (e.g. spatial resolution, energy

* Corresponding author.
** Corresponding author. Tel.: +86 1062767113.
E-mail addresses: yangkun9999@hotmail.com (K. Yang), renqsh@coe.pku.edu.cn (Q. Ren).

0168-9002/$ - see front matter © 2014 Elsevier B.V. All rights reserved.
http://dx.doi.org/10.1016/j.nima.2014.01.010

resolution, and sensitivity) and imaging results from phantom and animal studies are presented in order to evaluate the imaging performance of the PET imaging system.

2. Materials and methods

2.1. Instrumentation of the SiPM-based PET imaging system

2.1.1. PET imaging system geometry

The PET imaging system developed in this study consists of a stationary detector gantry, motor-controlled animal bed module, electronics modules, and power supply modules (see Fig. 1). The detector gantry is 655 mm high by 600 mm wide, and consists of 54 detector modules arranged in a ring with an inner diameter of 114 mm. The motor-controlled animal bed module is composed of an adjustable bracket, a motorized precision linear stage (WN250TA300L, Winner Optics, Beijing, China) and an animal bed. The animal bed can be moved along the axial direction by a servo motor (SGMAV-02ADA61+SGDV-1R6AO1A, Yaskawa Electric) that is controlled by a host PC. In addition, the vertical height can be adjusted manually. The animal bed is made from a transparent poly methyl methacrylate (PMMA) pipe and is designed to facilitate gas anesthesia. Limit and zero switches were installed and the animal bed can be controlled with a precision of 5 μm. The power supply consists of several direct-current (DC) power supply modules and a power supply circuit module that can output ± 5 V and ± 30 V. The entire PET imaging system can be set up on a 600×900 mm^2 optical table.

2.1.2. PET detector module

In this study, LYSO is the scintillator of choice for the detector due to its superior properties. Each PET detector block developed in this study has a LYSO (Yibo Industrials, Shanghai, China) scintillator block coupled to a 4×4 SiPM array (SPMArray4, SensL Inc., Cork, Ireland) through the optical silicone oil (see Fig. 2a). The SPMArray4 is a 16-element SiPM array that has a 3.16×3.16 mm^2 pixel chip area. Each pixel has a 3.05×3.05 mm^2 active area that contains 4774 microcells. The SiPM detectors are operated at an operating voltage of 30.0 V to achieve a pixel gain of about 2.4×10^6.

Each of the scintillator blocks has a 4×6 matrix of crystals [2.10 (± 0.05) mm $\times$ 3.16 (± 0.05) mm $\times$ 15 (± 0.1) mm]. The crystal surfaces are polished and the crystals are optically isolated from one another by reflective materials. The geometry of the PET detectors is shown in Figs. 2 and 3. Each PET detector block has a 4×6 LYSO scintillator block coupled to a 4×4 SiPM array. In the transaxial direction of FOV, each of the six LYSO crystals are coupled to four pixel chip areas of the SiPM array, as shown in Fig. 2b. Crystal type A, which are defined as a "full-coupled crystal", are fully coupled to 2/3 of the active area of the pixel chip, as well as crystal type B, which are defined as "half-coupled crystal", are coupled to both 1/3 active areas of two adjacent pixel chip areas. With a total of 54 detector blocks, the PET imaging system has eight crystal rings with 162 crystals per ring.

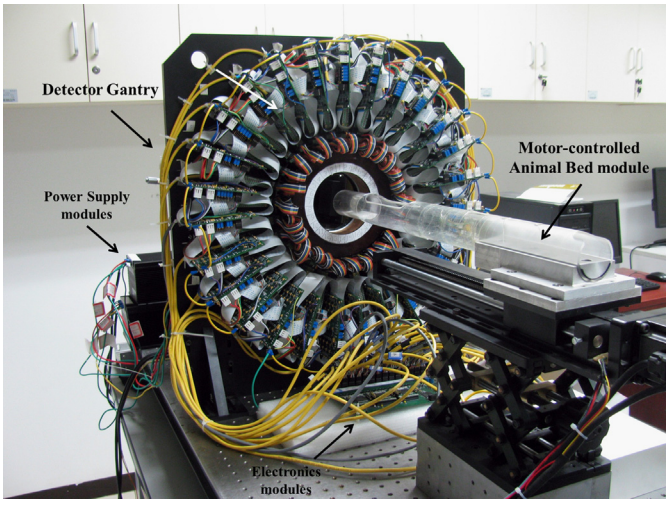

Fig. 1. The PET imaging system consisting of a stationary detector gantry, motor-controlled animal bed module, electronic modules, and power supply modules.

2.2. Electronics module design

In our design, the electronics module is composed of circuitry for pulse shaping, timing measurement, coincidence-detection, and communication, which play a role in amplifying position signals, constant fraction discriminator (CFD) of energy signals, time-to-digital converter (TDC) of the timing measurement, encoding of positional information, coincidence processing, data cache, and data transmission respectively (see Fig. 4). Each of the 27 detector banks needs its own standalone amplifier, timing measurement and position processing circuits, and all of the 27-channel signals are sent to the same coincidence processing circuit for position encoding and data transmission. The extensive use of field programmable gate array (FPGA) chips and TDC chips reduces the complexity of the circuits and improves design flexibility. Fig. 5 illustrates the signal processing architecture of the PET electronics module.

2.2.1. Pulse shaping circuitry design

The pulse shaping circuitry includes position signal and energy signal processing units. The position signals generated by the SiPM detectors are pulse signals. The amplitudes of the pulse signals can be amplified up to 1.5 V by the SPMArray4-A0 preamplifiers; the signal rise time is about 40 ns. Each pixel of the SiPM detector generates pulse signals when it detects photons. Consequently, each bank generates 32-channel position signals (each bank contains two blocks and each block generates 16-channel position signals) and each channel of the position signal has a positive and negative output.

The positive pulse signals are sent to a MAX907CSA, which is a dual channel, high-speed, ultra-low power voltage comparator, to compare with the position threshold voltage. When the amplitudes of the positive pulse signals are higher than the threshold voltage, MAX907CSA generates TTL-compatible outputs; otherwise, it generates zero signal. In addition, the threshold voltage of the position must be lower than the amplitude of the signals generated by the "half-coupled crystal"; otherwise these signals could be filtered out. However, a low threshold will increase system noise and sacrifice SNR. By using the MAX907CSA, all of the positive position signals are converted to digital signals and are then transferred to the timing measurement circuits to obtain positional information.

The negative position signals are summed to produce energy signals. By using an AD8045ARD operational amplifier, which is a unity gain-stable voltage-feedback amplifier with ultralow distortion, the energy signals are converted into positive signals with the waveform unchanged. The positive signals are then split into two channels and each signal is sent to a MAX913 chip, which is a single, high-speed, low-power comparators. Each channel signal is compared with the energy threshold voltage to filter the low energy signals, which are regarded as mixtures of noise, while the other channel signal is compared with the CFD threshold voltage to generate a timing pulse. Both of the processed signals are

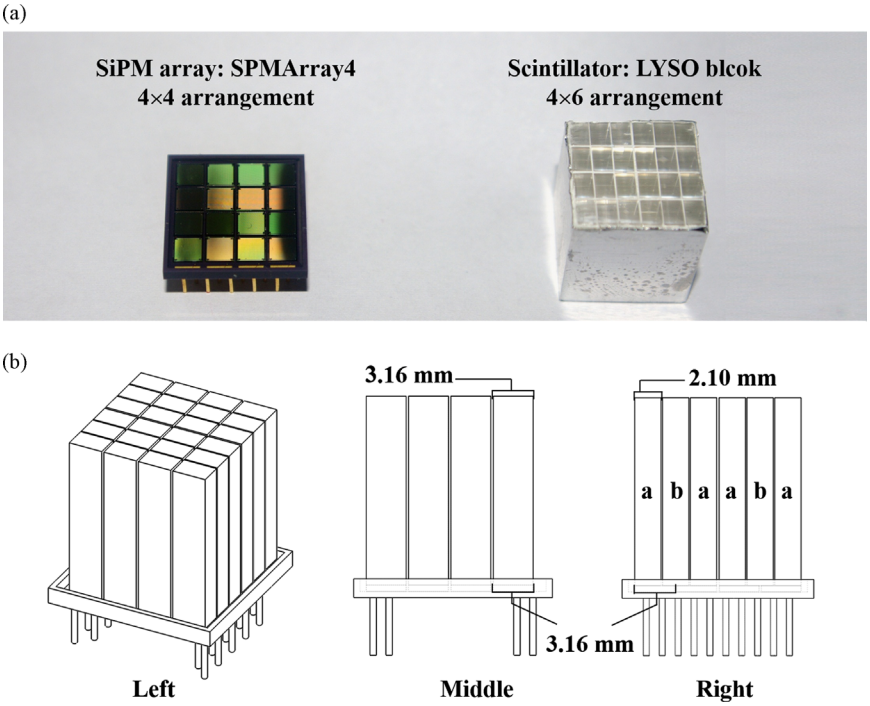

Fig. 2. Geometry of the PET detectors. (a) Each PET detector block developed in this study had a 4 × 6 LYSO scintillator block coupled to a 4 × 4 SiPM array. (b) Left: Schematic diagram of the detector block; Middle: Axial view of the detector block; Right: Transaxial view of the detector block.

transferred to the timing measurement circuitry in order to obtain timing information.

2.2.2. Timing measurement circuitry design

The timing measurement circuitry is mainly composed of two TDC chips (TDC-GP1, ACAM, Germany) and a FPGA chip (Cyclone – EP1C3T144C6, Altera, USA), as show in Fig. 4a. The TDC-GP1 is a universal 2-channel multi-hit time-to-digital converter that has two measurement channels with a typical resolution of 250 ps. In this study, the 2-channel TDC-GP1 chips were operated in resolution-adjust mode, in which the resolution of the two TDC-GP1 channels could be precisely adjusted to the same value. The resolution is decided only by the program and is not influenced by temperature or voltage. The external clock signals, which maintain long term stability, are provided by the FPGA chip. The power supply circuit of the TDC chips must be standalone. The TDC-GP1 chips measure the time interval between the timing pulse and time reference signal and then transform the time intervals into highest precision digital values. The FPGA chips are used to calculate the positional information of the position signals and then combine the positional information with the digital values of the time intervals in order to encode the position codes. The position codes are transformed into differential signals and then sent to the coincidence-detection circuitry.

2.2.3. Coincidence-detection circuitry design

The coincidence-detection circuitry is composed of several FPGA chips (Cyclone – EP1C3T144C6, Altera, USA) and their peripheral circuits, as shown in Fig. 4b. The FPGA chips set a coincidence time window that can be changed electronically from 1 to 64 ns in 1 ns steps, and was normally set to 12 ns in this study (i.e. a maximum timing resolution of 1 ns). In coincidence processing, the coincidence circuits successively check whether there are energy signals arriving at the coincidence circuit. If there are two energy signals arriving at the coincidence circuit within an interval that falls within the coincidence time window, they are deemed to be coincident events. Under these conditions, the position codes of the two energy signals will be regarded as coincidence event codes that are directly related to the geometry of the detector ring. Each crystal has its own crystal address code and each coincidence event code represents a line of response (LOR) of the detector ring. In data acquisition, the coincidence event codes are sent to a first in, first out (FIFO) cache and then transferred to a host PC for further processing. The communication processing is implemented by a reduced instruction set computer (RISC) microcontroller (S3C2440A, Samsung, Korea) through an Ethernet connection, as shown in Fig. 4c. Coincidence event data were stored in list mode format (LMF) on the host PC for coincidence decoding and image reconstruction. The axial FOV spans 26 mm, while the transaxial FOV is software-trimmed acquisition, resulting in a 60 mm transaxial FOV, which is sufficient to image small animals, such as mice. By interleaving LORs from adjacent angles, the sinogram matrix of the system has 192 projections per angle and a total of 162 projection angles. The system acquisition operates in 3D mode, permitting coincidences between two adjacent detector rings.

2.3. Performance characterization of the small animal PET imaging system

In this study, spatial resolution, sensitivity, time and energy resolution were evaluated based on the National Electrical Manufacturers Association (NEMA) NU-4 standards [22] and some articles [23–25]. Phantom and mice imaging studies were performed in order to evaluate the imaging performance of the PET system.

2.3.1. Spatial resolution

Spatial resolution was measured in a transaxial slice in both the radial and tangential directions. A capillary tube (0.5 mm inner diameter, 70 mm length) filled with 3.33 MBq (0.09 mCi) was located at one-fourth of the axial FOV from its center. At the following radial distances from the center of the PET imaging

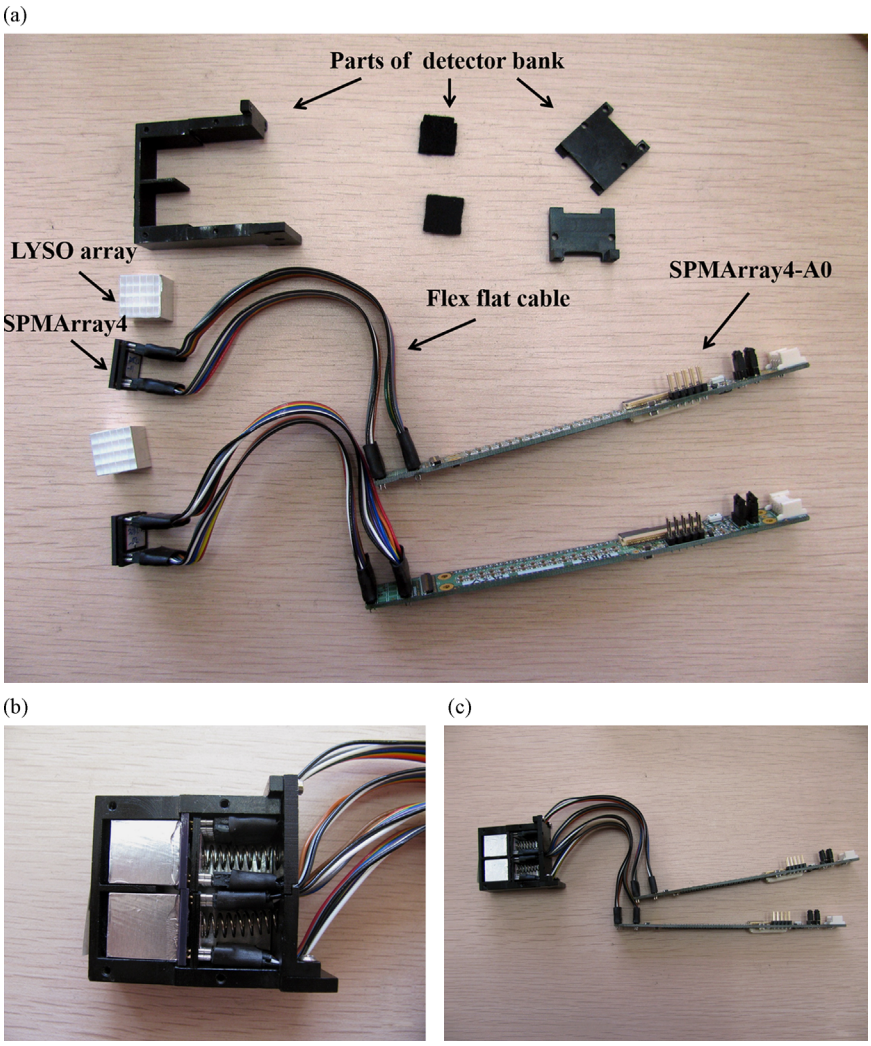

Fig. 3. Detector modules of the PET imaging system. (a) Exploded views of the detector bank. (b) Each bank has two blocks in the transaxial direction and each block contains a mechanical spring to guarantee tight coupling between the SiPM and scintillator array. (c) Each block is connected to an individual preamplifier using a 15 cm long flexible flat cable.

system FOV to the edge of the reconstructed FOV were applied: 1 mm, 5 mm, 10 mm, 15 mm, 20 mm, 25 mm, and 30 mm. In addition, the axial resolution was measured across transaxial slices by using a 0.777 MBq (0.021 mCi) ^{22}Na point source (0.5 mm diameter) conforming to the NEMA NU-4 standards at the following axial positions: 0–26 mm, in 2 mm steps. The imaging data were acquired for 2.0×10^5 counts and reconstructed by a filtered back-projection algorithm with no smoothing. The FWHM of the point source response function in transaxial and axial directions were calculated to demonstrate the spatial resolutions of the PET imaging system.

2.3.2. Sensitivity

The sensitivity of the PET imaging system was measured by using the ^{22}Na point source placed at the central locations of the axial and transaxial FOV. The source was stepped axially (0.5 mm steps) through the scanner to either end of the scanner's axial FOV, then returned to the initial central location and then stepped in the opposite direction to either end of the FOV. The data were acquired for 1 min to ensure that at least 10,000 true events were collected at each position, with a coincidence window of 12 ns and an energy window of 300–650 keV. The sensitivity (counts per second per Bq) was calculated as follows:

$$S_i = \frac{R_i - R_{B,i}}{A_{cal}}$$

where R_i and $R_{B,i}$ are the counting rate and background counting rate respectively, in counts per second. A_{cal} is the source activity, and as the branching ratio of ^{22}Na is 0.9060, the absolute sensitivity (percentage) is given by:

$$S_{A,i} = \frac{S_i}{0.9060} \times 100$$

2.3.3. Energy and timing resolutions

The ^{22}Na point source was located 55 mm in front of each PET detector bank that was connected to a 2048-channel output multichannel analyzer (EASY-MCA-2K, ORTEC, USA) which was used to acquire the energy and timing spectra data. The data were acquired for 5 min and calculated to demonstrate the energy and timing resolution performance.

2.3.4. Imaging performance

To evaluate the imaging performance of the PET imaging system, phantom and animal studies were performed. The detector bank

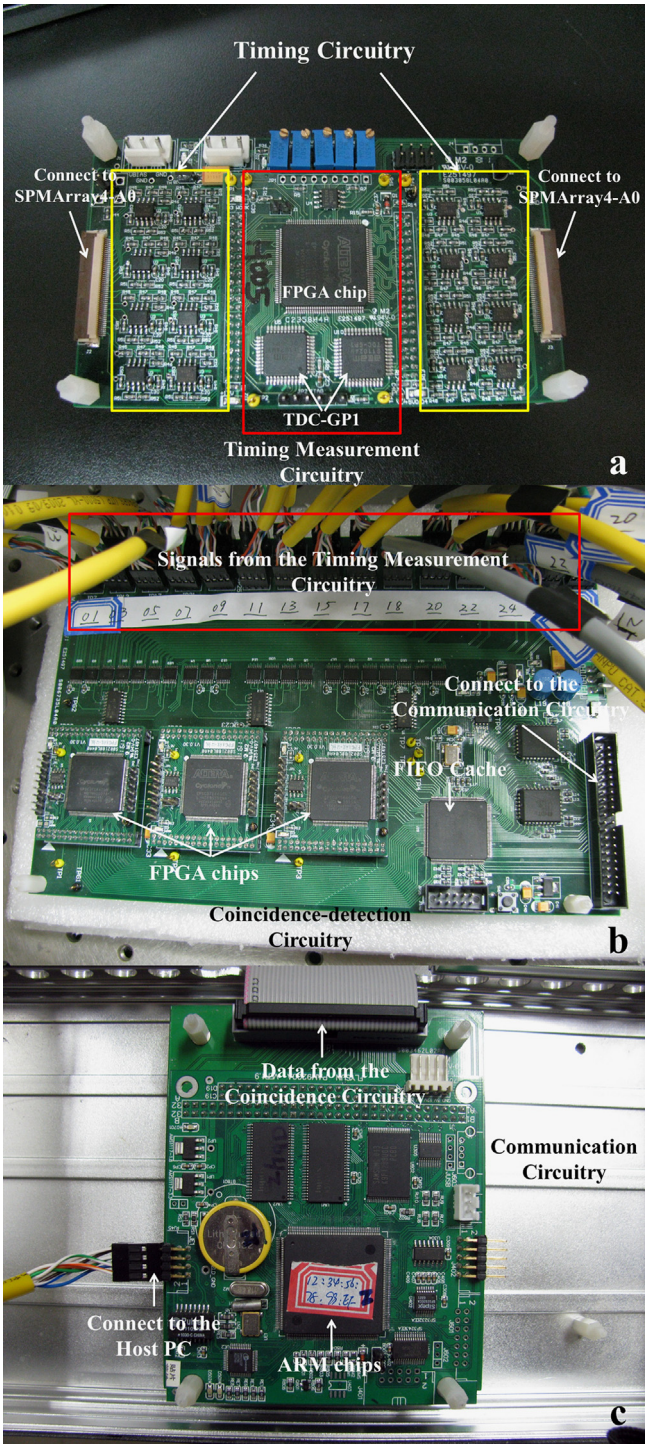

Fig. 4. Electronics modules of the PET imaging system. (a) Pulse shaping circuitry and timing measurement circuitry. (b) Coincidence-detection circuitry. (c) Communication circuitry.

modules were calibrated by using a ^{22}Na line source located at each detector to equalize the count rate. Three hot rod phantoms containing hot rods of different sizes (2.0, 2.5 and 3.0 diameter) were scanned in the PET imaging system. The center to center distance between adjacent rods is equal to the rod diameter. Each phantom was filled with 14.8 MBq (0.4 mCi) of ^{18}F-FDG and scanned for 10 min.

All PET imaging studies were performed in coincidence mode with an energy window of 300–650 keV and a coincidence window of 12 ns. All animals used were initially given a gas anesthesia of 3.00% isoflurane in oxygen to induce anesthesia and then were anesthetized by the continuous administration of 1.00% isoflurane in oxygen to prevent motion during the PET scanning. All animal studies were carried out in accordance with the guidelines from the Peking University Laboratory Animal Center and were reviewed and approved by this institution.

A 12-week, 25 g C57BL/6 male mouse, with a xenograft tumor [induced by hypodermic injection of a H22 mouse hepatoma cells (2.5×10^7, 2.5 ml) into the right leg] in its right leg, was intraperitoneally injected with 22.2 MBq (0.6 mCi) ^{18}F-FDG and after a 60-min uptake period was scanned for 40 min in four bed positions (10 min per bed position) to obtain a whole body PET image of the mouse. Then the mouse was sacrificed and the location of the tumor was confirmed and the tissue was removed for immunohistochemical analysis.

A 12-week, 22 g C57BL/6 male mouse, with a xenograft tumor [induced by intraperitoneal injection of H22 mouse hepatoma cells (2.5×10^7, 2.5 ml)] in its liver, was intraperitoneally injected with 18.5 MBq (0.5 mCi) ^{18}F-FDG and after a 60-min uptake period was scanned for 40 min in four bed positions (10 min per bed position) and a whole body PET image of the mouse was obtained. Then the mouse was sacrificed and the location of the tumor was confirmed and the tissue was removed for immunohistochemical analysis.

The sinogram data of the phantoms and animals were reconstructed by the algebraic reconstruction techniques (ART). Uniformity corrections of the axial direction were performed before the reconstruction using a correction factor array obtained by scanning the uniform ^{22}Na line source at the center of the FOV. For the animal imaging studies, images from the four bed positions were merged into one image with an axial coverage of 104 mm. To solve the imaging problem caused by the activity concentration in the region of the bladder, the bladder of each mouse was located at the fourth bed position and the region of interest (ROI) corresponding to the bladder was drawn to artificially limit the maximum value of the images in the other three bed positions.

3. Results

3.1. Spatial resolution, sensitivity, energy and timing resolution

Fig. 6 shows the axial and transaxial spatial resolutions in the radial and tangential directions of the PET imaging system as a function of the axial position and the radial distance from the center of the PET imaging system FOV, respectively. The reconstructed axial spatial FWHM resolution varies from 3.3 mm to 4.15 mm; the reconstructed transaxial spatial FWHM resolution in radial and tangential directions varies from 2.55 mm to 3.2 mm, and 2.575 mm to 3.225 mm, respectively.

Fig. 7 shows the sensitivity profile of the PET imaging system as a function of the axial position. The maximum sensitivity was 0.76% at the coincidence window of 12 ns and energy window of 300–650 keV. Despite the edge of the axial FOV, the center has the similar poor sensitivity performance because of the 3 mm dead space between the two detector blocks in each detector bank.

Fig. 8 shows the flood histogram of a typical detector bank, timing spectrum and two representative energy spectra of the detector crystals in this bank. The timing resolution of the prototype PET is 1.3 ns. The energy resolution across all crystals in the PET imaging system, which could have better performance in the full-coupled crystals, and worse performance in the half-coupled crystals, as shown in Fig. 8, ranged from 14.0% to 30.5% with a mean of 21.0%.

3.2. Imaging performance

Fig. 9 shows the transaxial images of the hot rod phantoms, which demonstrate that the PET imaging system can resolve rods

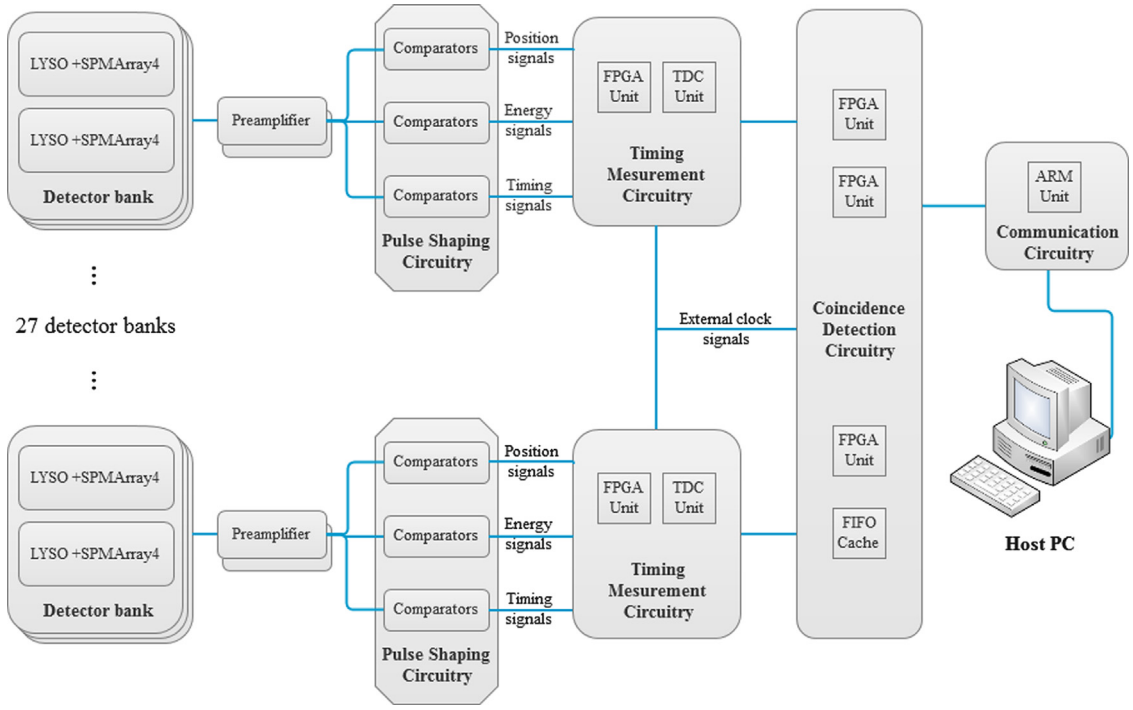

Fig. 5. The signal processing architecture of the PET electronics module.

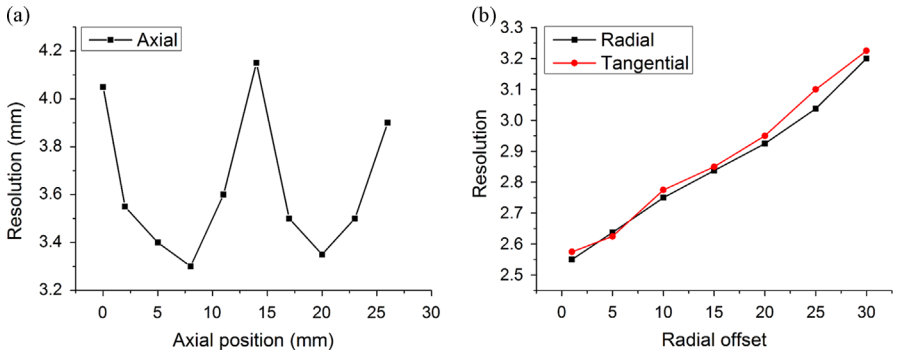

Fig. 6. Image spatial resolutions, measured with a ^{22}Na point source (0.5 mm in diameter). (a) Axial spatial resolution as a function of the axial position of the PET imaging system. (b) The transaxial spatial resolution in the radial and tangential directions as a function of the radial distance from the center of the PET imaging system FOV.

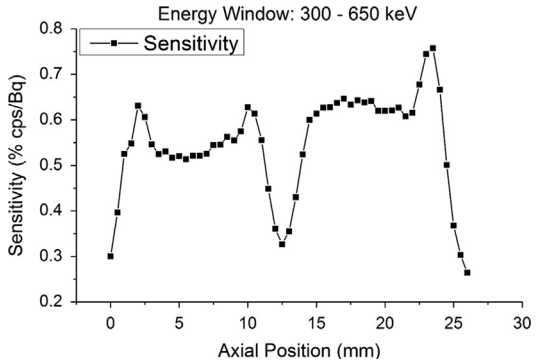

Fig. 7. The sensitivity profile of the PET imaging system as a function of the axial position. Measured with a ^{22}Na point source (0.5 mm in diameter).

with a diameter of 2.5 mm and above rods in the phantom by using ART reconstruction algorithm.

Fig. 10 shows the whole body images of the 25 g C57BL/6 mouse with a xenograft tumor in its right leg. Transaxial, coronal and sagittal images of the mouse are illustrated. The 12 mm diameter tumor was then removed and examined *ex vivo*, which reveal liquefaction necrosis in the interior of the tumor consistent with the PET images. The activity accumulation of ^{18}F-FDG was not evident in the bladder because the mouse urinated before the PET scanning and the urine was removed.

Fig. 11 shows whole body images of the 22 g C57BL/6 mouse with a xenograft liver tumor. Transaxial, coronal and sagittal images of the mouse are illustrated. The radioactivity accumulation in the abdomen of the mouse was evident in all PET images, which indicated the tumor's location. The 3 mm diameter tumor tissue, which can be seen in the liver, confirmed the PET images results.

4. Discussion

We have developed a compact PET imaging system based on SiPM detectors. When using the motorized precision animal bed module, the PET imaging system can obtain whole body images of small animals. It benefits from the designs of the detector and electronic modules, in which a radial spatial resolution of 2.55 mm can be achieved at the center of the FOV. However, poor

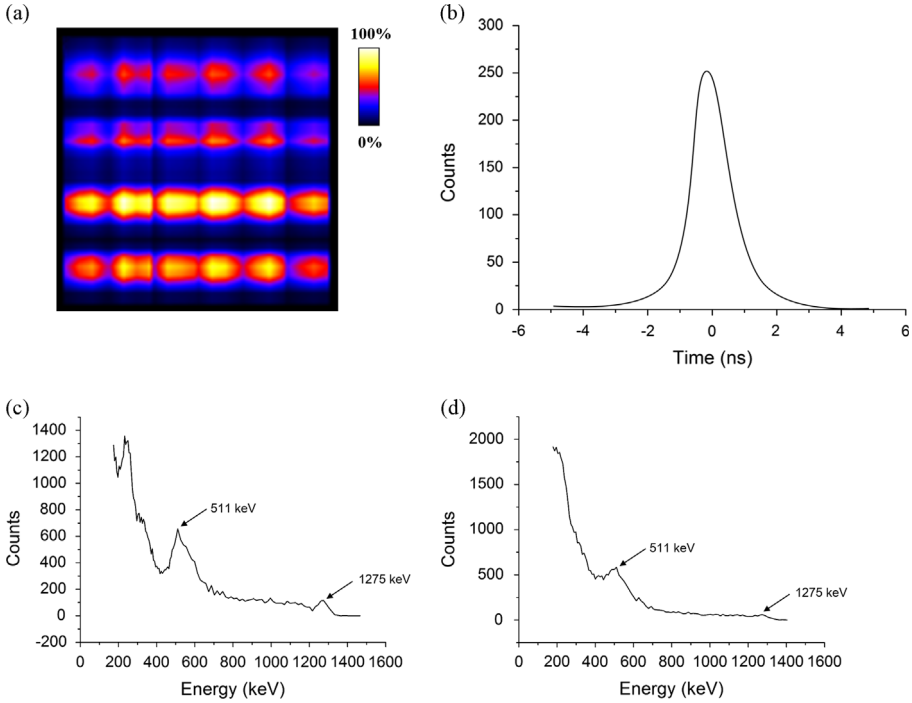

Fig. 8. Energy and timing performances of a typical detector bank. (a) Flood histogram of a typical detector block. (b) Timing spectrum of one detector channel. (c) The best energy resolution performance of this detector block. (d) The worst resolution performance of this detector block.

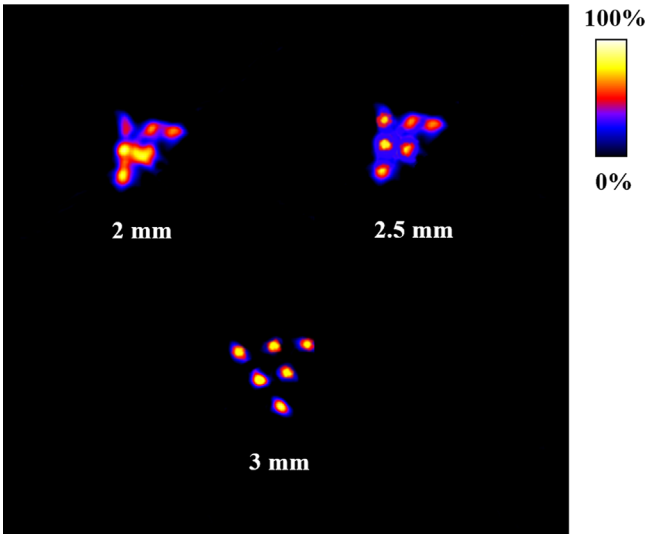

Fig. 9. Transaxial images of hot rod phantoms. The diameters of the hot rods were 2.0, 2.5, and 3.0 mm. The center to center distance between adjacent rods is equal to the rod diameter.

performance of the electronic signal noise can degrade the imaging performance of the PET system. In addition, the radial spatial resolution was degraded at edge of the FOV due to the parallax error caused by the gamma rays obliquely incident to the scintillator surface at that location. The degradation can be improved by using appropriate reconstruction methods or by measuring the depth of interaction (DOI) of the detectors. These issues are currently being studied.

The energy resolution of the PET imaging system is 21% on average, which is slightly worse than some commercial PMT based animal PET systems [24] and another SiPM based PET scanner [21]. The energy resolution performance of the half-coupled crystals was worse, and could be as low as 30.5%. The main reason for this was that the energy peak position of the half-coupled crystals were relatively low and part of the energy peak has an overlap with the energy peak formed by Compton scattering. The performance of the energy resolution can be increased by improving the electronic modules. In this study, the electronic modules used energy threshold voltages adjusted by potentiometers in order to recognize the energy peaks and the low energy threshold voltage, and this caused the overlap between the energy peak position of the half-coupled crystals and the Compton scattering, and can introduce a lot of noise into the electronic modules. The noise can lead to not only energy resolution issues but also sensitivity issues that are caused by significantly increased scattered coincidence rates. Improvement can be achieved by using energy peak measurements in the electronics modules. Because the background noise of SiPM is a little higher than traditional PMTs, the electronics module should have the ability to achieve a high level of noise interference suppression. For example, the use of the TDC-GP1 can achieve very high timing resolution ($\sim$1 ns in this study), but requiring the FPGA chips to provide high precision clock sequences, and needing individual power supply circuit to avoid the noise crosstalk.

In the animal studies, we found that the spatial resolution was also a short coming of the PET imaging system, especially in the axial direction. The four sides of the SPMArray4 have a 1.33 mm width dead space, and for each detector bank the dead space between two blocks can be about 3 mm. We used an interpolation method to create a new virtual slice between the two actual slices at the edges of the blocks. However, in this case the imaging performance of the central axial FOV can be degraded (as shown in Figs. 6a and 7). In further research, we will incorporate the use of light guides into the device, which should minimize the dead space between blocks for better performance.

The sensitivity profile (as shown in Fig. 7) is not consistent with fully 3D acquisition. This issue is caused by the dead space and only coincidences between two adjacent detector rings. In animal studies, sensitivity becomes another issue in our PET imaging system. Due to the low sensitivity, the PET imaging system

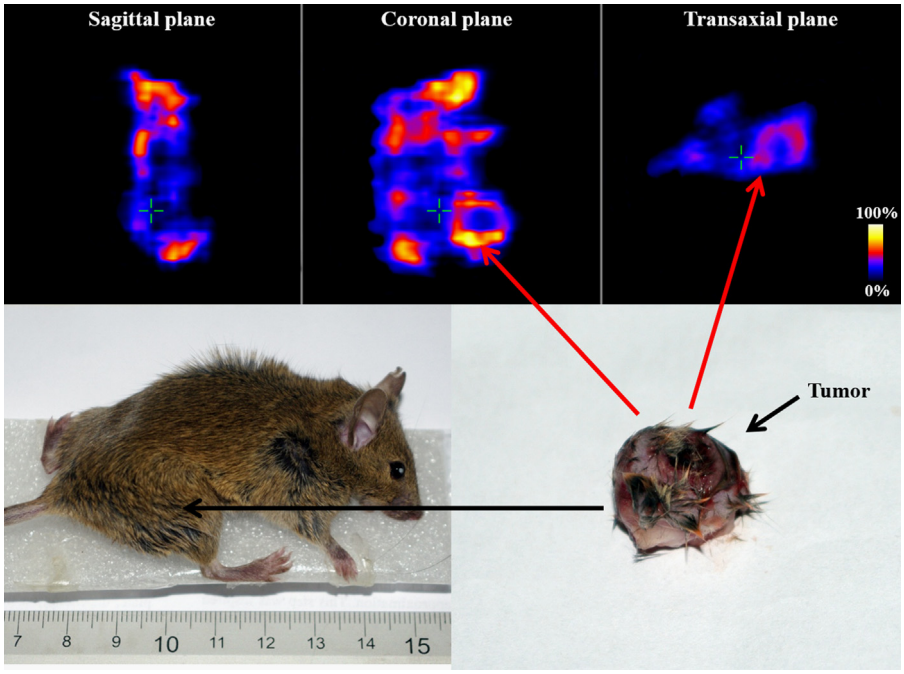

Fig. 10. Tumor imaging of a 25 g C57BL/6 mouse with an implanted tumor in its right leg. The transaxial, coronal and sagittal images of the mouse are illustrated. The tumor (arrow) is 12 mm in diameter with liquefaction necrosis in the internal parts, consistent with the PET images.

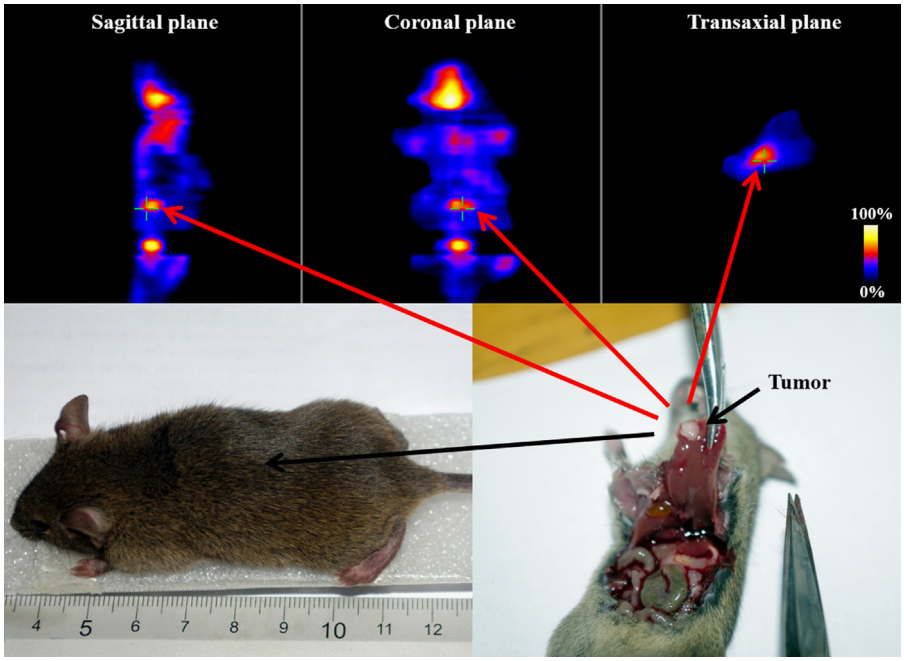

Fig. 11. Tumor imaging of a 22 g C57BL/6 mouse with an implanted tumor in its liver. The transaxial, coronal and sagittal images of the mouse are illustrated. The tumor (arrow) was 3 mm in diameter and could be seen in the PET images.

required a long scanning duration (20 min or more per bed position) to obtain high quality PET images, although shorter scanning times, such as 10 min, are also acceptable. Although increasing the axial FOV increases the device cost, it can reduce the scanning time, and the SiPM detectors have the potential to become low-cost photo sensors because they can be manufactured using a standard complementary metal-oxide-semiconductor (CMOS) process.

Without the appropriate scattering, attenuation and dead time correction, the imaging in this paper only provides a qualitative measure of image quality. Iterative reconstruction algorithms such as ART have been successfully applied to the PET imaging system and have demonstrated very promising results. Due to the small dimensions and low operating voltage, the PET system is compactly designed, which could be integrated into a multi-modality imaging system. The performance evaluations we have conducted for the PET system suggest that the SiPM detector can be an appropriate substitute for PMTs in PET systems. Clearly, more improvements of the PET imaging system need to be done. We will improve the performance by employing newly designed electronics modules, using smaller crystals and state-of-art SiPMs with a smaller detector size and better performance, as well as using

improved PET detector geometry that can address the depth of interaction. We plan to develop another SiPM-based PET imaging system with improved imaging performance in the near future.

5. Conclusion

We have developed a compact, lightweight SiPM-based PET imaging system that has a 60 mm transaxial FOV and 26 mm axial FOV. The system has a spatial FWHM resolution of 2.55–3.225 mm in the transaxial FOV and 3.3–4.15 mm in the axial FOV, an on average energy resolution of 21%, and a maximum sensitivity of 0.76% at a coincidence window of 12 ns and an energy window of 300–650 keV. Phantom imaging and tumorous ^{18}F-FDG imaging in mice demonstrated the imaging performance of the PET imaging system. These results from performance tests and imaging studies demonstrate the feasibility of an animal PET system based on SiPM detectors and indicate that SiPM detectors could be promising photodetectors in animal PET instrumentation development.

Acknowledgments

This work is supported by The National Key Instrumentation Development Project (2011YQ030114), The National Basic Research Program of China (973 Program, 2011CB707500), National Natural Science Foundation of China (11104058), and Natural Science Foundation of Hebei Province (A2011201155). The authors acknowledge the helpful support of Peking University Laboratory Animal Center.

References

[1] C.S. Levin, H. Zaidi, PET Clinics 2 (2007) 125.
[2] B.J. Pichler, H.F. Wehrl, M.S. Judenhofer, Journal of Nuclear Medicine 49 (2008) 5S.
[3] H. Zaidi, R. Prasad, Advances in multimodality molecular imaging, 2009.
[4] T.K. Lewellen, Physics in Medicine and Biology 53 (2008) R287.
[5] B.H. Peng, C.S. Levin, Current Pharmaceutical Biotechnology 11 (2010) 555.
[6] H. Zaidi, A. Del Guerra, Medical Physics 38 (2011) 5667.
[7] P. Buzhan, B. Dolgoshein, L. Filatov, A. Ilyin, V. Kantzerov, V. Kaplin, A. Karakash, F. Kayumov, S. Klemin, E. Popova, S. Smirnov, Detectors and Associated Equipment 504 (2003) 48.
[8] D. Renker, Detectors and Associated Equipment 567 (2006) 48.
[9] I. Britvitch, I. Johnson, D. Renker, A. Stoykov, E. Lorenz, Detectors and Associated Equipment 571 (2007) 308.
[10] E. Roncali, S.R. Cherry, Annals of Biomedical Engineering 39 (2011) 1358.
[11] D. Renker, Journal of Instrumentation 5 (2010) P01001.
[12] S. Yamamoto, H. Horii, M. Hurutani, K. Matsumoto, M. Senda, Annals of Nuclear Medicine 19 (2005) 109.
[13] J. Kang, Y. Choi, K.J. Hong, W. Hu, J.H. Jung, Y. Huh, B.-T. Kim, Journal of Instrumentation 6 (2011) P08012.
[14] H. Peng, P.D. Olcott, V. Spanoudaki, C.S. Levin, Physics in Medicine and Biology 56 (2011) 3603.
[15] S.J. Hong, H.G. Kang, G.B. Ko, I.C. Song, J.-T. Rhee, J.S. Lee, Physics in Medicine and Biology 57 (2012) 3869.
[16] H.S. Yoon, G.B. Ko, S.I. Kwon, C.M. Lee, M. Ito, I. Chan Song, D.S. Lee, S.J. Hong, J. S. Lee, Journal of Nuclear Medicine 53 (2012) 608.
[17] S. Yamamoto, H. Watabe, Y. Kanai, M. Imaizumi, T. Watabe, E. Shimosegawa, J. Hatazawa, Physics in Medicine and Biology 56 (2011) 7555.
[18] T. Yamaya, T. Mitsuhashi, T. Matsumoto, N. Inadama, F. Nishikido, E. Yoshida, H. Murayama, H. Kawai, M. Suga, M. Watanabe, Physics in Medicine and Biology 56 (2011) 6793.
[19] S. Yamamoto, M. Imaizumi, T. Watabe, H. Watabe, Y. Kanai, E. Shimosegawa, J. Hatazawa, Physics in Medicine and Biology 55 (2010) 5817.
[20] S.I. Kwon, J.S. Lee, H.S. Yoon, M. Ito, G.B. Ko, J.Y. Choi, S.H. Lee, I. Chan Song, J. M. Jeong, D.S. Lee, S.J. Hong, Journal of Nuclear Medicine 52 (2011) 572.
[21] J.H. Jung, Y. Choi, K.J. Hong, J. Kang, W. Hu, H.K. Lim, Y. Huh, S. Kim, J. Jung, K. B. Kim, Medical Physics 39 (2012) 1227.
[22] N.E.M.A. (NEMA), Performance Measurements for Small Animal Positron Emission Tomographs (PETs): NEMA, NEMA Standards Publication NU, Rosslyn, VA, 2008 (4-2008).
[23] Y.C. Tai, A. Chatziioannou, S. Siegel, J. Young, D. Newport, R.N. Goble, R.E. Nutt, S.R. Cherry, Physics in Medicine and Biology 46 (2001) 1845.
[24] Y.-C. Tai, A. Ruangma, D. Rowland, S. Siegel, D.F. Newport, P.L. Chow, R. Laforest, Journal of Nuclear Medicine 46 (2005) 455.
[25] A.L. Goertzen, Q. Bao, M. Bergeron, E. Blankemeyer, S. Blinder, M. Cañadas, A. F. Chatziioannou, K. Dinelle, E. Elhami, H.-S. Jans, E. Lage, R. Lecomte, V. Sossi, S. Surti, Y.-C. Tai, J.J. Vaquero, E. Vicente, D.A. Williams, R. Laforest, Journal of Nuclear Medicine 53 (2012) 1300.